science.sciencemag.org/content/366/6462/221/suppl/DC1

Supplementary Materials for

Spatial control of heavy-fermion superconductivity in $CeIrIn_5$

Maja D. Bachmann*, G. M. Ferguson*, Florian Theuss, Tobias Meng, Carsten Putzke, Toni Helm, K. R. Shirer, You-Sheng Li, K. A. Modic, Michael Nicklas, Markus König, D. Low, Sayak Ghosh, Andrew P. Mackenzie, Frank Arnold, Elena Hassinger, Ross D. McDonald, Laurel E. Winter, Eric D. Bauer, Filip Ronning, B. J. Ramshaw, Katja C. Nowack†‡, Philip J. W. Moll†‡

*These authors contributed equally to this work.
†These authors contributed equally to this work.
‡Corresponding author. Email: philip.moll@epfl.ch (P.J.W.M.); kcn34@cornell.edu (K.C.N.)

Published 11 October 2019, *Science* **366**, 221 (2019)
DOI: 10.1126/science.aao6640

This PDF file includes:

Materials and Methods

Single Crystal Growth:

$CeIrIn_5$ single crystals were prepared using an indium flux method following the recipe described elsewhere (3). Cubic, mm-sized crystals with clear faces following the crystal directions resulted from the growth. The crystal orientation was confirmed using Laue X-ray diffraction prior to the FIB structuring. While some macroscopic crystals show clearly visible intergrowth of excess indium, these regions can be easily avoided in the microstructuring process. Accordingly, we can exclude the incorporation of elementary indium inclusions in our crystalline microstructures: 1) We do not observe resistive anomalies in the microstructures at the $T_c \approx 3.4$ K of elementary indium; and the critical field of the type-I superconductor In is much lower than the critical fields observed in our microstructures (Fig. 3). Within the SSM images, we have not found any evidence for material inhomogeneity, which would be easily detectable as a deviation between the simulated T_c patterns and the observed data.

FIB Fabrication:

The fabrication procedure consists of three main steps. First a slab of typical dimensions 100 µm × 20 µm × 3 µm is cut from the crystal at high ion currents (10-20 nA) and subsequently slightly surface polished down to the targeted thickness at lower currents (1-3 nA). This slab is then transferred onto epoxy glue (Araldite brand) on a sapphire substrate with predefined gold leads. Contacts to the slab are made by sputtering gold through a shadow mask, which is subsequently patterned into the contact geometry in another FIB step. Finally, the desired device shape is patterned at low currents (0.3-0.7 nA). The active parts of the devices, for example the resistance bars between the voltage contacts, are further polished at 80 pA to obtain vertical sidewalls and reduce any over-spray contamination from the patterning process. Two FIB machines were used for this study. Most devices were fabricated using a Ga-based FIB (FEI Helios G3). To exclude any artefacts from Ga-contamination, some were fabricated using a Xe-based FIB (FEI Helios PFIB G4). The acceleration voltage was kept constant at 30 kV on both systems. A more detailed description and step by step protocol of the sample fabrication has been published elsewhere (9).

Scanning SQUID microscopy:

To identify superconductivity in the sample we use a well characterized scanning SQUID susceptometer (26) operated in a dilution refrigerator. The SQUID features a pickup loop with a 1.5 µm inner and 3.2 µm outer diameter and a concentric field coil with a 6 µm inner and 12 µm outer diameter. Applying a low-frequency ac current excitation to the field coil generates a local magnetic field near the pickup loop. The same current flows through a secondary field coil, coupling flux into a counterwound secondary pickup loop located ~1 mm from the sample surface. The counterwound

design ensures that the net flux coupled into the SQUID loop is dominated by the susceptibility of the sample. The susceptibility signal is recorded with a standard lockin amplifier. We subtract a constant offset from all images that corresponds to the residual flux coupled into the SQUID by the field coil due to lithographic imperfections. A superconductor will screen the magnetic field from the field coil, which is detected as a diamagnetic susceptibility by the SQUID. The SQUID is operated in a flux locked loop, such that the SQUID response is linear in the flux through the pickup loop with a well-characterized slope.

To construct an image, we scan the susceptometer parallel to the sample surface at an estimated height of ~1-3 μm while recording the local susceptibility of the sample. When the SQUID scans over a superconducting region of the sample, we detect the diamagnetic response from the Meissner effect, allowing us to distinguish superconducting regions of the sample from insulating and metallic regions. By taking a series of images at a range of temperatures through the superconducting transition, we track the development of superconductivity with micrometer scale spatial resolution.

For all presented images, a current of ~100 μA was applied to the field coil at a frequency of approximately 100 Hz. We have checked that the images do not qualitatively change with the excitation amplitude in this range. In some images we have simultaneously applied a current to the device at a different frequency to record transport characteristics. We have verified for all presented images that the applied currents were low enough to not qualitatively change the susceptibility images. A typical image shown here is recorded within 30 to 60 minutes.

For images and transport on the lamella, device 1 and device 2, the recorded temperature is the temperature of the mixing chamber plate in the dilution refrigerator. The sample is anchored to the mixing chamber through a solid copper cold finger. The scanner is home-built from piezoelectric elements. The two scan directions are not perfectly orthogonal causing a slight distortion in the images. This causes features in the susceptibility images to appear slightly distorted.

Measurement of $CeIrIn_5$ Elastic Moduli:

A single crystal of $CeIrIn_5$ oriented along the crystallographic axes was polished to dimensions 0.79 mm×1.06 mm×1.14 mm, with 1.14 mm along the c axis. Resonant ultrasound experiments were performed in a custom-made apparatus, where the sample is held in weak contact between two compressional mode lithium niobate transducers (see (27) for details) Fig. S10 shows the lowest-frequency vibrational resonances measured at room temperature. Each resonance frequency is uniquely determined by the sample dimensions, density and elastic moduli, and can be calculated by solving the 3D elastic equation (28). To determine the elastic moduli from the resonances we solve the inverse problem following the procedure outlined in (27). The elastic moduli at 295 K (in GPa) are listed in Table II. From the moduli, we calculate the bulk modulus B= 82.23 GPa and linear compressibilities $\kappa_a = 4.01\times10^{-3}$ GPa^{-1}, $\kappa_c = 4.13\times10^{-3}$ GPa^{-1}, which are in reasonable agreement with the values reported in (11) (B= 87.6 GPa, $\kappa_a = 3.44\times10^{-3}$ GPa^{-1}, $\kappa_c = 3.48\times10^{-3}$ GPa^{-1})

Finite Element Method Simulations:

For each sample geometry we perform finite element method (FEM) simulations to determine the strain field induced through the differential thermal contraction between the sapphire substrate and the $CeIrIn_5$ microstructure. The FEM simulations are performed using the Structural Mechanics Module in COMSOL Mutiphysics® (29). For each device, we construct a 3D model of the $CeIrIn_5$ microstructure and anchor it to a sapphire substrate using a thin layer of epoxy (see Fig. S5). Although the $CeIrIn_5$ is unstrained at room temperature in our calculations, the mismatch in thermal expansion between $CeIrIn_5$ and the sapphire substrate generates a strain field when the devices are cooled to cryogenic temperatures. The sapphire substrate is cut along (0001). In the simulations we assume sapphire to be mechanically isotropic.

In the simulation, there are two interfaces that must be constrained by appropriate boundary conditions: the interface between the sapphire and the epoxy, and the interface between the epoxy and the $CeIrIn_5$. We assume that when the device is assembled at room temperature, the stress on the $CeIrIn_5$ is negligible, which we model as a zero-stress boundary condition at room temperature. To model the adhesion between the sapphire, epoxy and $CeIrIn_5$, we require that the strain field is continuous at each interface.

Although the changes in the elastic moduli of $CeIrIn_5$ and the sapphire substrate are small when cooled to cryogenic temperatures, the elastic modulus of the Araldite 5 minute epoxy changes from 3.4 GPa at room temperature to 7.2 GPa at liquid nitrogen temperature (30). We verified that the quantitative results of the FEM calculations are insensitive to the elastic modulus of the epoxy layer by tuning the modulus of the epoxy in the simulation between 1.6 GPa and 9.2 GPa. Within this range of values, the predicted T_c on the device varies by at most 10 mK (see Fig. S9).

We assume that the epoxy layer is 200 nm thick, which is consistent with a typical thickness obtained by our sample preparation. In order to understand the role the mechanical properties of the epoxy plays in determining the strain in the microstructures, we repeat the finite element method simulations while systematically varying the thickness and elastic modulus of the epoxy layer, computing a T_c map for each combination. We present the results of this calculation for each of the microstructures in Fig. S9. We find that increasing the thickness gradually attenuates the strain field in the $CeIrIn_5$ microstructure. However, the spatial pattern is preserved for epoxy layers as thick as ≈ 2 μm.

In real samples, it is possible that the epoxy bonds to the edges of the crystal in addition to the bottom surface. To understand the role that the epoxy geometry plays in determining the induced strain field, we performed simulations in which the $CeIrIn_5$ microstructure is embedded in a glue disk. When the microstructure is embedded in a disk of epoxy, the strain field along the edges of the microstructure is modified, but the qualitative behavior is unchanged. For simplicity, we present simulations with only a bottom layer of epoxy in the manuscript.

Using the parameters outlined in table S1, we compute the strain at each point in the finite element grid. In Voigt notation, the strain is a 6 dimensional vector,

$$\vec{\varepsilon} = (\varepsilon_1\ \varepsilon_2\ \varepsilon_3\ \varepsilon_4\ \varepsilon_5\ \varepsilon_6)$$

Using the coordinate system defined by the crystallographic axes of the $CeIrIn_5$ crystal, the first three components ε_1, ε_2, ε_3 correspond to the uniaxial strains ε_a, ε_b, ε_c. As

an example for the strain fields resulting in the microstructures, Fig. S6 shows the six components of the simulated strain tensor at the top surface of the unprocessed lamella. Figures S7 and S8 show the six components of the strain tensor at the top surface of device 1 and device 2 respectively.

Supplementary Text:

Crystalline Quality of the Microstuctures:

The crystalline quality of the FIB-prepared microstructures was carefully checked. First, the obtained resistivity values and the temperature dependence of the resistivity are in quantitative agreement with previous reports measured on macroscopic crystals. Both the residual resistivity ratio R(300 K)/R(2 K) = 17 and the residual resistivity $\rho_a(2K) \approx 2\ \mu\Omega$ cm are in quantitative agreement with measurements on macroscopic single crystals (31), suggesting that no significant crystal defects were introduced during the fabrication procedure (Fig. S1).To further investigate the crystalline properties of the microstructures, quantum oscillation experiments have been performed. We do observe large Shubnikov-de Haas(SdH) oscillations above 8 T in the microstructures (Fig.4). The high quality of the microstructures is evidenced by the large Fermi surface sections of several kT observed in the SdH oscillations. In addition, a low frequency band dispersing from 270 T for H||[001] to 460 T for H||[100] is clearly observed. This was previously reported as the γ-branch, hosting the lightest electrons in $CeIrIn_5$. Figure 4 contrasts the frequencies observed in a microstructure (data points) to those reported from deHaas-van Alphen measurements of magnetic quantum oscillations by Haga et al. (4). The agreement of the angle-dependent frequency spectrum is remarkable and indicates that $CeIrIn_5$ can be microstructured without deterioration of the crystal quality. To the best of our knowledge, this is the first report of Shubnikov-de Haas oscillations in $CeIrIn_5$. FIB microstructuring can strongly increase the total device resistance due to the large geometrical factors achievable in microbars. In macroscopic crystals of such good conductors, prohibitively large currents for dilution-refrigerator temperatures are required to resolve the small resistance modulation due to the density of states oscillations.

Reproducibility:

In order to exclude experimental artifacts based on the new fabrication process, total of 11 structures were fabricated (including the lamella). Of these 3 were imaged by SSM, 8 were characterized using only electronic transport and 1 was imaged and characterized in transport simultaneously. Figure S2 B-D and figure S3 show structures and their basic transport characteristics that were not shown in the main manuscript. Below we describe the purpose of each structure. As measurements in a dilution refrigerator are very time consuming and only limited time on these machines were available, the bulk of these measurements were performed in a ^{3}He system with a nominal base temperature around 400 mK. Therefore, some of the transitions to a zero-resistance state were not observable in these measurements if the local strain profile suppresses the transition temperature too strongly. All the devices that were measured to lower temperatures did consistently show a sharp transition to zero resistance between any terminals.

In the following, we present a series of different structure designs, aimed to uncover the limitations of the strain field generation. Interestingly, all are in agreement with the results obtained in simpler geometries presented for clarity in the main manuscript.

No evidence for inhomogeneous superconductivity along a: Whenever spatial modulations of the order parameter are allowable or desired, a main question concerns the degree of control of the spatial modulation. To that end, the structure in Figure S2B probes the transport along the a-direction over macroscopic length scales. With a total length of 220 μm along a, this longest transport bar extends into macroscopic dimensions, and is about one order of magnitude longer than the structures of the main manuscript. Yet despite this macroscopic length, no sign of a superconducting transition is detected within the long bar. If strong strain gradients beyond the known biaxial tensile strain were present in the device, for example due to buckling in 3D or other motion not captured in our simulation, one would expect a local modulation of T_c over this distance. Yet this is not observed, indicating that the pressure remains homogeneous across such large length scales. This is further supported by the remarkable similarity of both bars aligned with the c-direction, on either end of the device. Despite their large distance, the transition in both is virtually identical, evidencing that both ends of the device experience virtually identical strain fields.

Different Crystals: As the typical single crystals of $CeIrIn_5$ used as the starting material for the microfabrication are mm-sized, in principle thousands of structures can be made from one crystal. To avoid any sample dependence, we have used different crystals from multiple batches for this study and all give consistent results. The device shown in Figure S2C was fabricated from the same crystal made by J. Sarrao for a transport study (31) which had been stored in air for more than 10 years. Yet the results are in good agreement with those taken on three fresh crystals obtained from two new growth batches. This further corroborates the absence of structural inhomogeneity inside the sample, and supports this clean materials class as reliable for robust fabrication of structures.

Gallium Contamination: The liquid metal ion source (LMIS) has been a key development in the field of ion sources, and Ga-based FIBs have become the standard in commercial devices. While their high resolution is a significant advantage for microstructuring, at the same time all specimens will be slightly contaminated by Ga on the surface. It may be conceivable that surface reactions of this Ga with Ce, Ir, In and air lead to a formation of a superconducting surface shell. In particular, the Ga-rich layer may respond differently to strain and change our results quantitatively. The high critical current density observed in the devices, as well as the scaling of the upper critical field of all transitions presented in the main manuscript already provides strong evidence that the main physical phenomena are not due to Ga-interactions.

Nonetheless, to completely eliminate any spurious influence of Ga, we fabricated the structure in Figure S2D entirely Ga-free by using Xe-ion beams. Xe is known to completely desorb from solids and does not lead to permanent implantation. Even if $CeIrIn_5$ would be among the rare cases of materials able to capture Xe, it could not participate in the formation of metallic bonds and superconductivity. Plasma-based Xe

ion sources exhibit high flux density at reasonably well focused spots and are ideally suited for coarse cutting in the 10 µm range. To achieve spots focused tightly enough to fabricate microstructures, the ion current has to be greatly reduced. This structure was cut at 100 pA for 10 h. It has never been exposed to any Ga beam, and no change is observed in its behavior.

Systematic fabrication artefacts: Most microstructures were carved from a face orthogonal to the crystal c-direction, therefore the short edge of the sample is aligned with the c-direction and the long one is along a. This opens the possibility of unknown sources of systematic errors. The device shown in Figure S3E was cut from a face orthogonal to a, thus reversing the directions of the axes of the microstructure. Therefore, all fabrication steps for this structure are rotated by 90° with respect to the crystal axis. Every process step was rotated by 90°, and any fabrication-based anisotropy should now be reversed, but the results are unchanged. This sample excludes any potential fabrication-biased artefact that induces superconductivity always along the long edge of the device. The phenomenology perfectly follows the crystal axes, and not the device orientation.

This furthermore supports the notion of a biaxial strain field that is transmitted homogeneously into the crystal structure. The shape anisotropy of the devices themselves is captured in the calculations, yet the orientation of the crystal devices may lead to additional biased artefacts not captured in the 2D simulations. This establishes that the relative orientation between the $CeIrIn_5$ lamella and the sapphire crystal is indeed not relevant, a fact that strongly simplifies the fabrication.

Etching Bulk Samples:

In bulk $CeIrIn_5$ samples the resistive transition T_c^* is commonly reported between 0.8 K and 1.2 K, which is significantly higher than the thermodynamic phase transition at $T_c = 0.4$ K. Our results suggest a microscopic explanation for this phenomenology, with strain-induced patches of superconductivity emerging at the surface due to wiresawing bulk crystals.

An important step is now to relate our results on microstructures to those on macroscopic crystals. To that end, 5 bar shaped devices were cut by a wire saw from a high quality single crystal. Typical bar dimensions are 300 µm × 300 µm × 1500 µm. The samples were contacted by a combination of argon etching (5 min, 200 V, 12 mA) and gold sputter deposition (100 nm) onto the contact areas. Silver wires (25 µm diameter) were attached using silver epoxy (Epotek EE129-4) and cured for 1 h at 100°C. To prevent any extrinsic stress, the samples were not glued onto a substrate but held in place by the four silver wires alone.

All wire sawed samples show an enhanced superconducting transition at $T_c^* \approx 1$ K. The samples were then dipped in 11% hydrochloric acid (HCl) for 10-15 min, until a change of the surface color was clearly visible under a microscope (see Fig. S4B). This procedure leaves the normal state resistivity unchanged, whereas the superconducting transition drops to close to the thermodynamically expected value of 400 mK. This behavior was consistently seen across all 5 samples. These observations are consistent

with interpreting T_c^* observed in non-etched samples to be a result of surface strain induced by sample preparation, in particular by the commonly used wire-saw. Upon etching, the strained layer is removed and the T_c^* superconductivity vanishes. This clearly excludes an intrinsic mechanism to increase T_c around intergrowth defects akin to the 3K-phase around eutectic Ru-inclusions in Sr_2RuO_4 (32), but shows the 1K-phase of $CeIrIn_5$ to be a surface defect phenomenon. Our results furthermore show the FIB fabrication to be a much gentler technique compared to sawing or polishing, as no additional surface strain is induced by the ion milling. To showcase this explicitly, a macroscopic crystal was first etched until no transition was observed above 400 mK. Afterwards, the same crystal was patterned using a Xenon FIB (500 nA). The resistive transition remained unchanged, demonstrating that ion milling does not induce strained surfaces unlike wire sawing.

Role of Shear Strain:

In our devices, the shear strains ε_{ab} and ε_{bc} are an order of magnitude smaller than ε_a throughout the device. The shear strain ε_{ac} is also substantially smaller than ε_a, except in small regions near narrow constrictions in devices 1 and 2. In order to understand the coupling of the shear strain components to the superconducting transition temperature, we follow (33) and turn to a Ginzburg- Landau free energy approach. In the absence of strain, the Ginzburg-Landau free energy takes the form:

$$F = A(T - T_c)|\eta|^2 + f_4(\eta)$$

Where T is the temperature, T_c is the superconducting transition temperature η is the order parameter, and A is a coupling constant. The term $f_4(\eta)$ represents all fourth-order terms containing η which respect the symmetry of the system. To model the effects of strain on T_c, we add terms to the free energy F_{strain}, demanding that each term be invariant under all symmetry transformations of the system:

$$F_{strain} = \sum_i \Lambda_i \varepsilon_i \mathcal{V}_i + \frac{1}{2}\sum_i c_i \varepsilon_i^2 + c_{13}\left(\varepsilon_{A1g,1}\right) \times \left(\varepsilon_{A1g,2}\right) \qquad (S1)$$

Here we include terms that couple the order parameter η in second order, the strain ε in first order and the elastic energy of the lattice. The ε_i are the components of the strain field, Λ_i are the coupling constants between the order parameter and the associated strain field. $\mathcal{V}_i$ is a bilinear form of η with the same symmetry as the strain field ε_i. The c_i are the elastic moduli of the sample. In a tetragonal lattice, the strain ε_i breaks into five irreducible representations:

$$\varepsilon_{A_{1g,1}} = \varepsilon_a + \varepsilon_b$$
$$\varepsilon_{A_{1g,2}} = \varepsilon_c$$
$$\varepsilon_{B_{1g}} = \varepsilon_a - \varepsilon_b$$
$$\varepsilon_{B_{2g}} = 2\varepsilon_{ab}$$
$$\varepsilon_{E_g} = \{2\varepsilon_{ac}, 2\varepsilon_{bc}\}$$

Given that η in $CeIrIn_5$ belongs to a one-dimensional representation of the D_{4h} point group symmetry (34, 35, 36), the order parameter couples exclusively to the two A_{1g} representations of the strain field in the elastic free energy with the bilinear $\mathcal{V}_i = |\eta|^2$ in eq. S1 (33). To first order in the strain fields, shear strains ε_{ab}, $\varepsilon_{ac}, \varepsilon_{bc}$ do not couple to the order parameter and do not change T_c because they belong to the B_{2g} and E_g representations respectively.

T_c Maps:

We use the simulated strain profile to compute the superconducting critical temperature T_c on the FEM grid. The pressure and strain dependence of T_c can be written to leading order (27, 32),

$$T_c = T_{co} + \frac{\delta T_c}{\delta \varepsilon_a}\varepsilon_a + \frac{\delta T_c}{\delta \varepsilon_b}\varepsilon_b + \frac{\delta T_c}{\delta \varepsilon_c}\varepsilon_c$$
$$T_c = T_{co} + \frac{\delta T_c}{\delta P_a}P_a + \frac{\delta T_c}{\delta P_b}P_b + \frac{\delta T_c}{\delta P_c}P_c \qquad (S2)$$

Where $\delta T_c/\delta \varepsilon_i$ is the change in the critical temperature of the superconductor in response to uniaxial strain along the i axis. Similarly, $\delta T_c/\delta P_i$ is the change in T_c in response to uniaxial pressure along the i axis. We have excluded higher order terms in the expansion for the critical temperature due to the linear relationship between T_c and uniaxial pressure in $CeIrIn_5$ (5).

To proceed we need the three $\delta T_c/\delta \varepsilon_i$ for $CeIrIn_5$. We can compute these using the elastic constants of $CeIrIn_5$ (see Methods) and the change in T_c under uniaxial pressure (5, 6). As outlined in the previous section, we assume the effects of shear strain on T_c is weak and approximate:

$$\vec{P} = \begin{pmatrix} P_a \\ P_b \\ P_c \\ 0 \\ 0 \\ 0 \end{pmatrix}, \ \vec{\varepsilon} = \begin{pmatrix} \varepsilon_a \\ \varepsilon_b \\ \varepsilon_c \\ 0 \\ 0 \\ 0 \end{pmatrix}, \ \frac{\overrightarrow{\delta T_c}}{\delta P} = \begin{pmatrix} \delta T_c/\delta P_a \\ \delta T_c/\delta P_b \\ \delta T_c/\delta P_c \\ 0 \\ 0 \\ 0 \end{pmatrix}, \ \frac{\overrightarrow{\delta T_c}}{\delta \varepsilon} = \begin{pmatrix} \delta T_c/\delta \varepsilon_a \\ \delta T_c/\delta \varepsilon_b \\ \delta T_c/\delta \varepsilon_c \\ 0 \\ 0 \\ 0 \end{pmatrix}$$

Combining these definitions with eq. S2 we can write the change in the critical temperature ΔT_c,

$$\Delta T_c = \vec{P} \cdot \frac{\overrightarrow{\delta T_c}}{\delta P} = \vec{\varepsilon} \cdot \frac{\overrightarrow{\delta T_c}}{\delta \varepsilon}.$$

We write the stress-strain relationship for the solid as $\vec{\varepsilon} = S\vec{\sigma}$, where σ is the stress and S is the compliance tensor. The compliance tensor is determined by the elastic constants C_{ij}, for a tetragonal crystal, S takes the form,

$$S = \begin{pmatrix} C_{11} & C_{12} & C_{13} & 0 & 0 & 0 \\ C_{12} & C_{11} & C_{13} & 0 & 0 & 0 \\ C_{13} & C_{13} & C_{33} & 0 & 0 & 0 \\ 0 & 0 & 0 & C_{44} & 0 & 0 \\ 0 & 0 & 0 & 0 & C_{44} & 0 \\ 0 & 0 & 0 & 0 & 0 & C_{66} \end{pmatrix}^{-1}$$

In an ideal uniaxial pressure experiment $\vec{P} = -\vec{\sigma}$ throughout the sample volume. In this case we can write,

$$-\vec{\sigma} \cdot \frac{\overrightarrow{\delta T_c}}{\delta P} = (S\,\vec{\sigma}) \cdot \frac{\overrightarrow{\delta T_c}}{\delta \varepsilon}.$$

Multiplying both sides by $S^{-1} = C$ gives,

$$-\left(\mathrm{C}\frac{\overrightarrow{\delta T_c}}{\delta P}\right) \cdot \vec{\sigma} = \frac{\overrightarrow{\delta T_c}}{\delta \varepsilon} \cdot \vec{\sigma}.$$

This implies that ΔT_c from applied pressure and ΔT_c from applied strain are simply related by the elastic constants of the material,

$$-\left(\mathrm{C}\frac{\overrightarrow{\delta T_c}}{\delta P}\right) = \frac{\overrightarrow{\delta T_c}}{\delta \varepsilon}.$$

Using room temperature measurements of the elastic constants of $CeIrIn_5$ (see Methods: Measurement of $CeIrIn_5$ Elastic Moduli) and the measured $\delta T_c/\delta P_i$ (5, 6) we calculate,

$$\delta T_c/\delta \varepsilon_{a,b} = -57K, \qquad \delta T_c/\delta \varepsilon_c = 66K.$$

We use these values to compute the local T_c in our device from the simulated strain profile on the FEM grid.

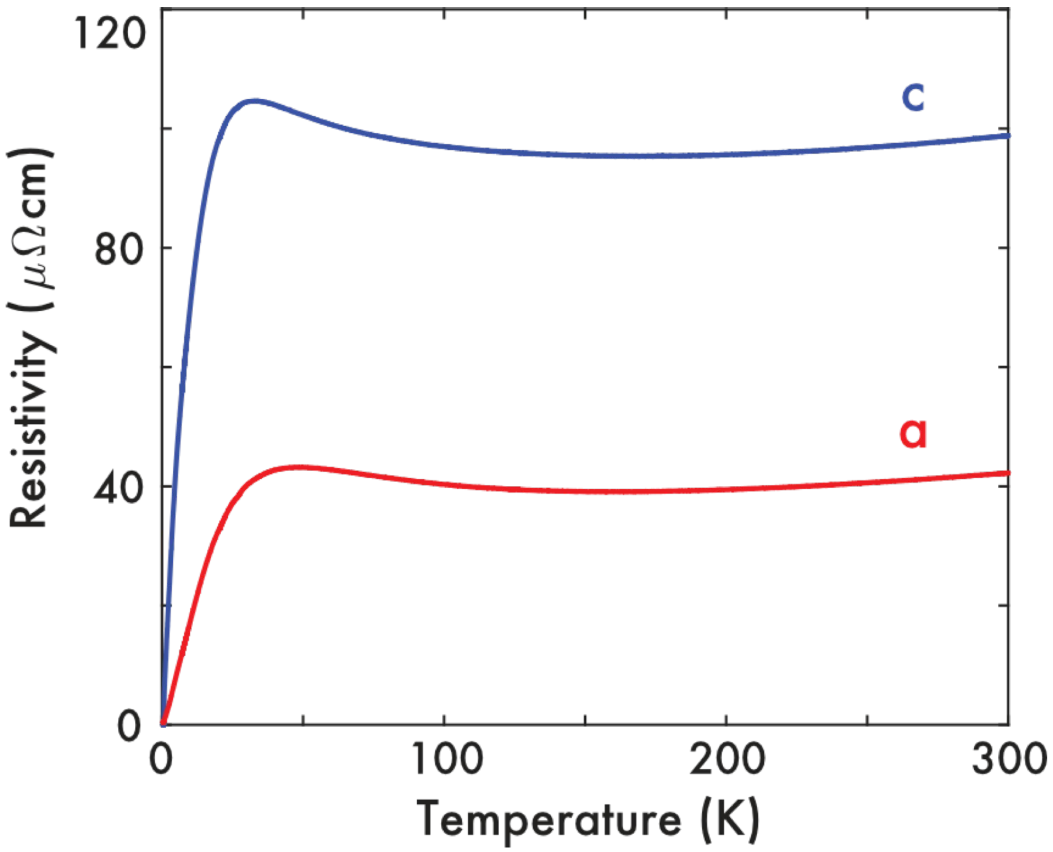

Fig. S1.
Temperature-dependence of the resistivity in the microstructures. The observed residual resistivity indicates that the fabrication procedure does not introduce a significant number of defects.

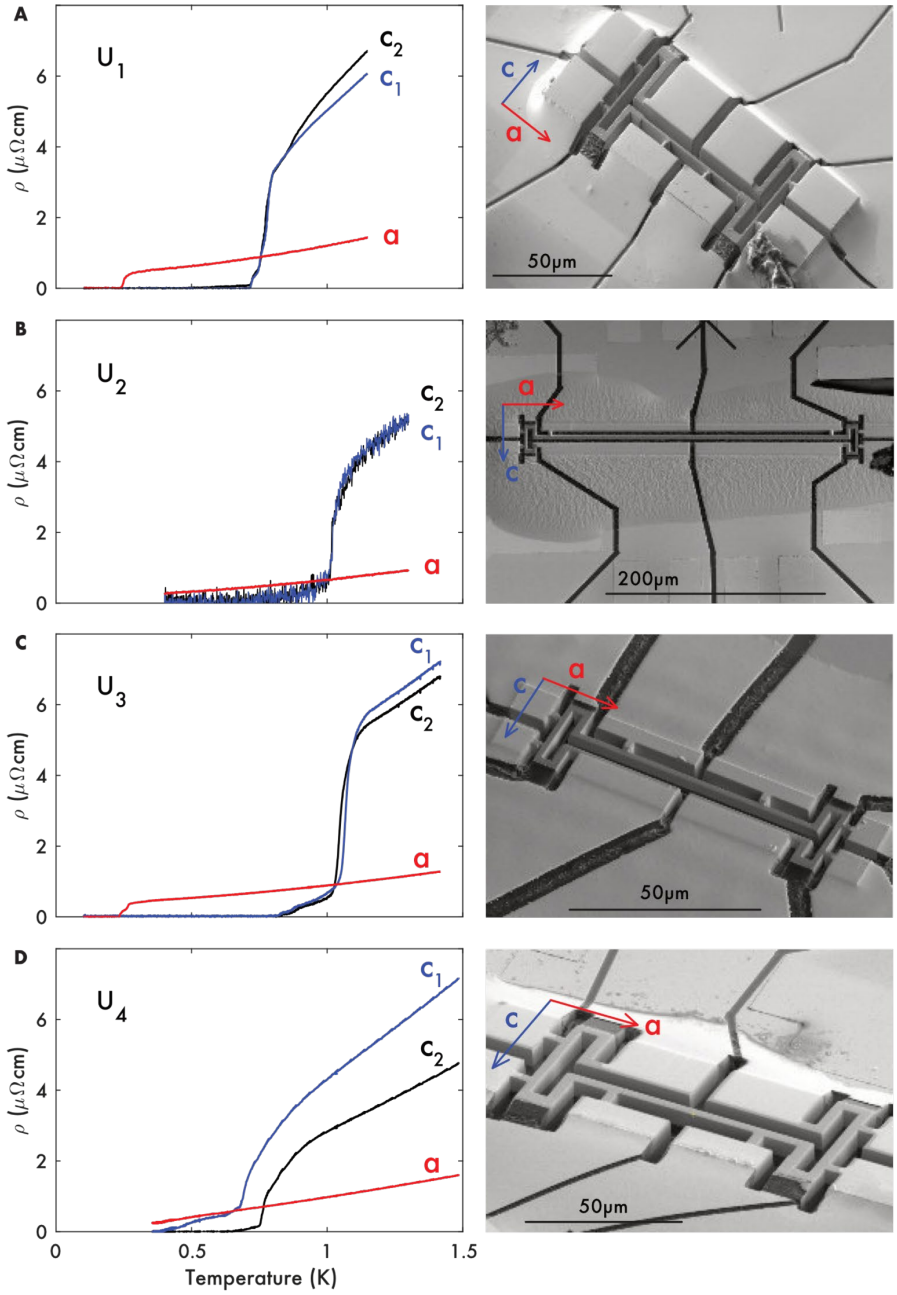

Fig. S2

Overview of microstructures designed to probe the modulation of superconductivity in electrical transport. In many different microstructures we observe the same qualitative transport phenomena. A transition to a zero-resistance state for beams aligned with the crystallographic c-axis is observed at a substantially higher temperature than for beams aligned with the crystallographic a-axis.

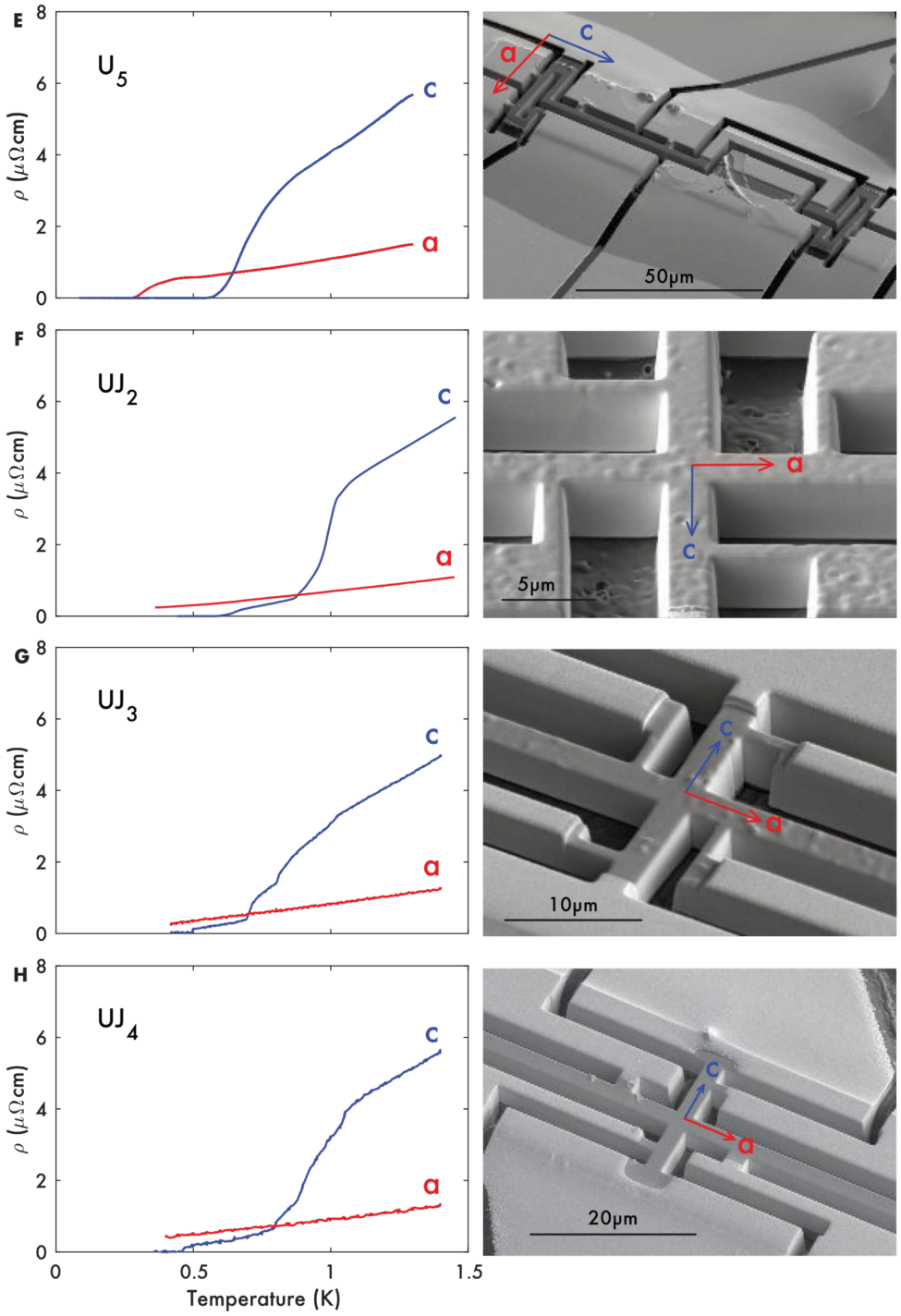

Fig. S3

Additional microstructures designed to probe the modulation of superconductivity in electrical transport. In cross-shaped structures we observe a transition to a zero-resistance state for beams aligned with the crystallographic c-axis, while the a-axis resistance remains finite, indicating that one arm of the cross contains a continuous superconducting path while the other arm does not.

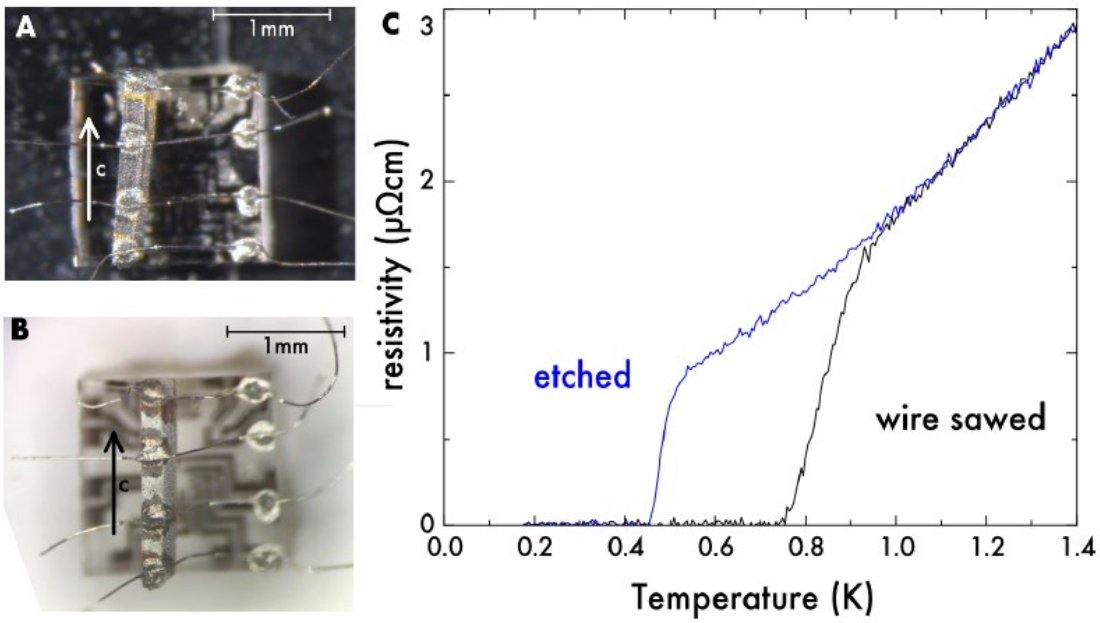

Fig. S4.

Photograph of a wire-sawed bar sample before (A) and after (B) HCl etching. In panel B a clear change in surface roughness can be seen where the crystal has been attacked by the acid (light grey areas). (C) Resistivity of a bulk bar sample right after wire sawing and after etching. The normal state resistivity remains the same while the superconducting transition is reduced and becomes sharper upon etching.

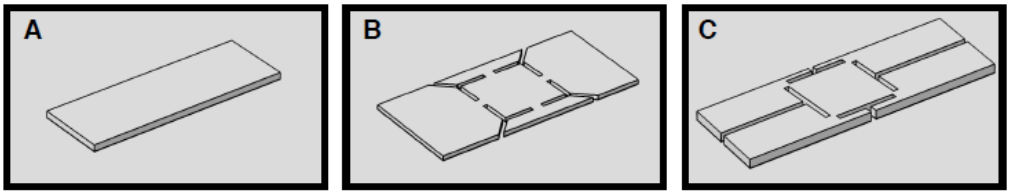

Fig. S5

3D models of (A) the lamella, (B) device 1 and (C) device 2 used for finite element method calculations. The dimensions of the structures are matched to the physical dimensions of the three samples measured with scanning SQUID microscopy.

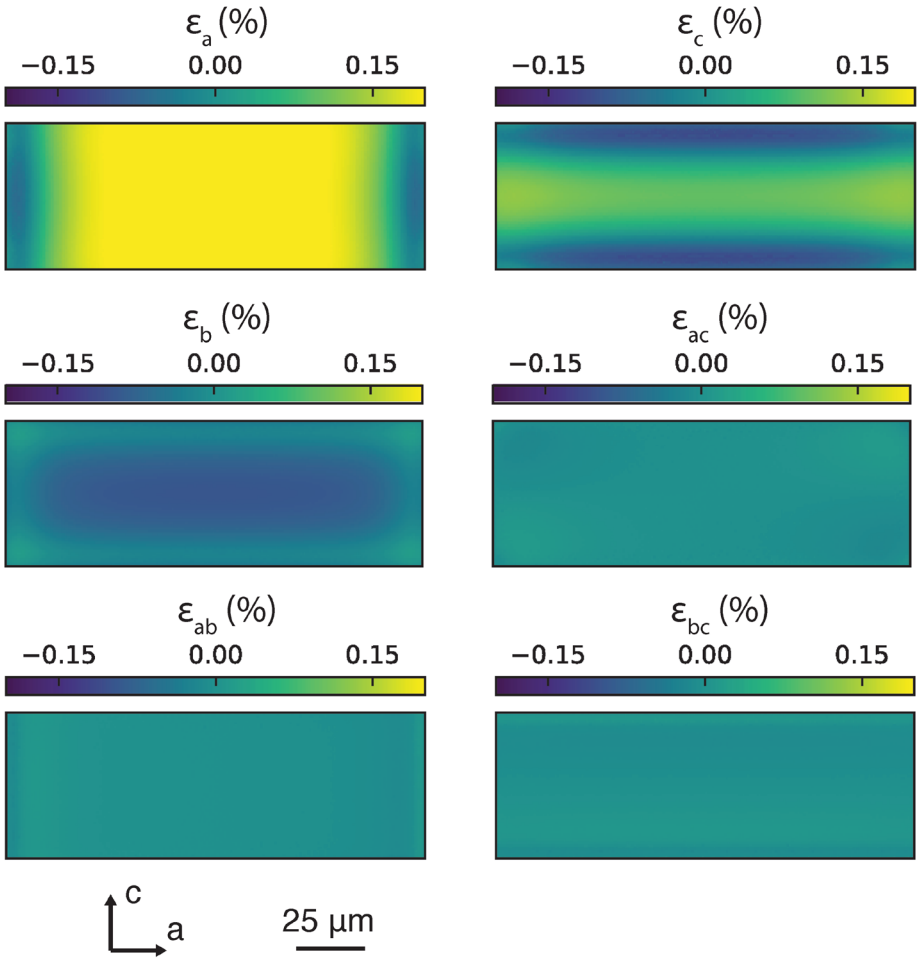

Fig. S6

Six components of the of the strain tensor at the top surface of the lamella, calculated using finite element method simulations. The c-axis of the crystal is aligned with the short edge of the lamella; the a-axis of the crystal is aligned with the long edge.

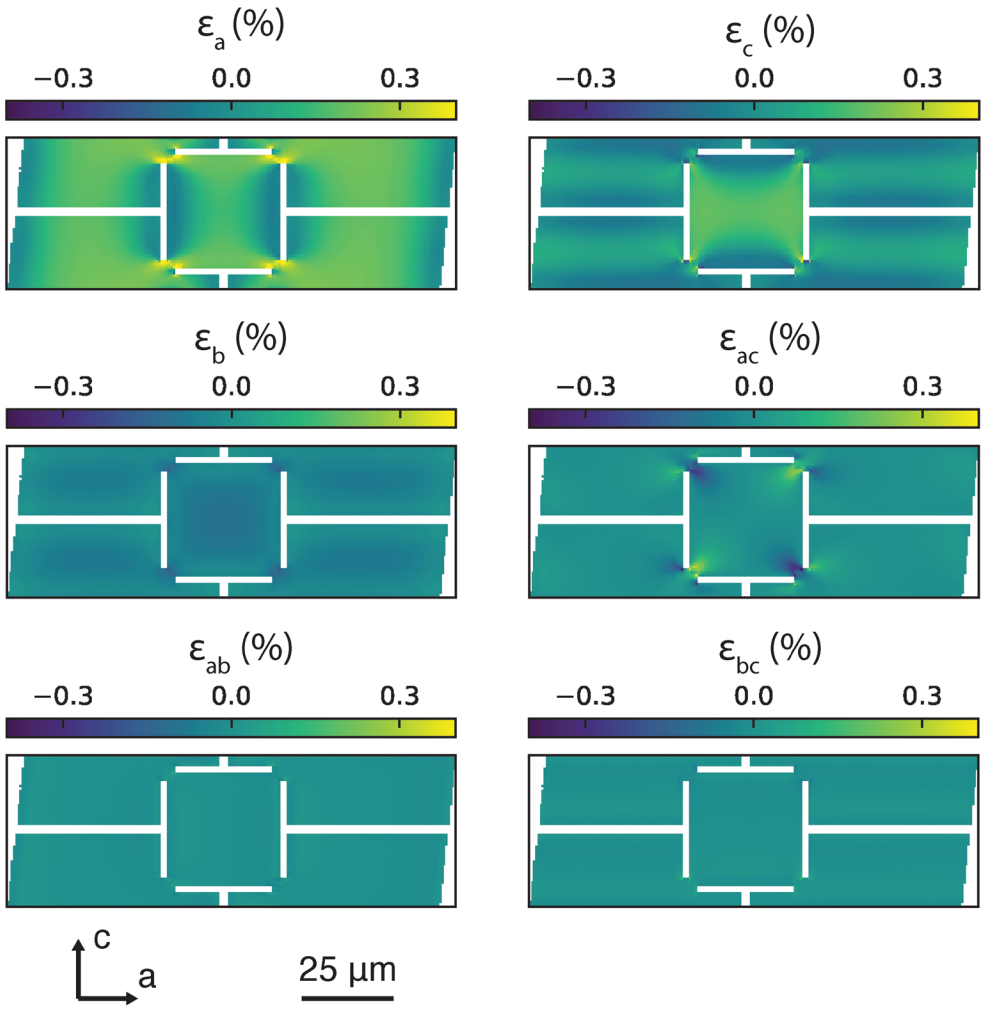

Fig. S7

Six components of the strain tensor at the top surface of device 1, calculated using finite element method simulations. The c-axis of the crystal is aligned with the short edge of the device; the a-axis of the crystal is aligned with the long edge of the device.

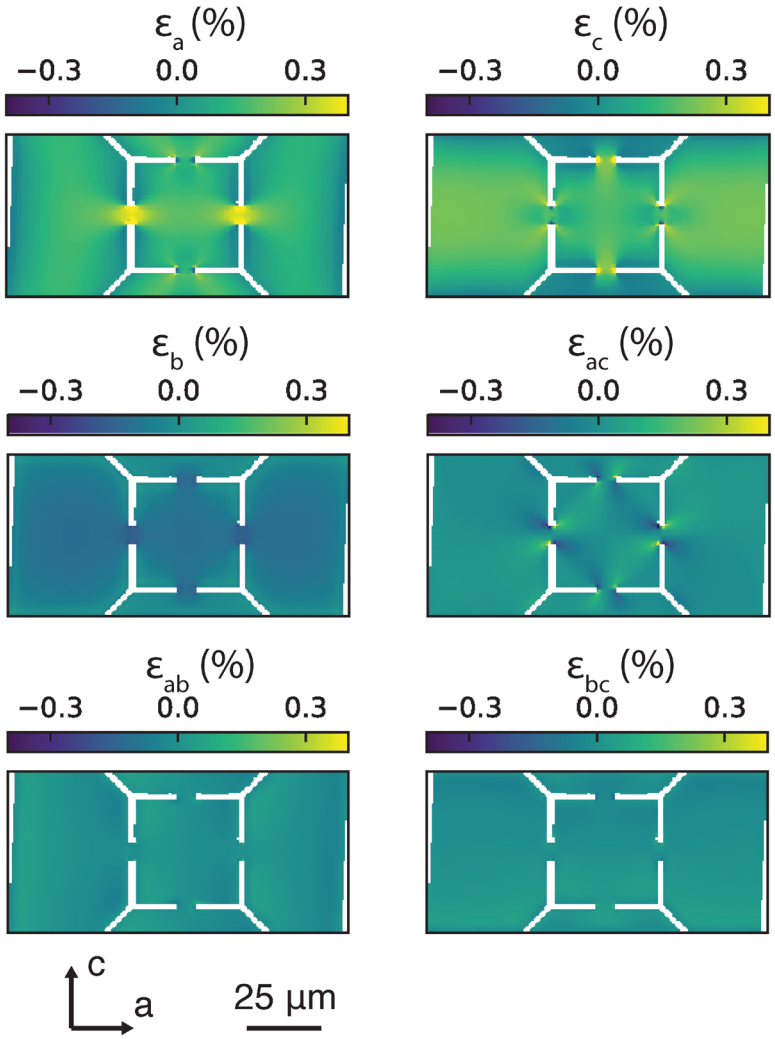

Fig. S8

Six components of the strain tensor at the top surface of device 2, calculated using finite element method simulations. The c-axis of the crystal is aligned with the short edge of the device; the a-axis of the crystal is aligned with the long edge of the device.

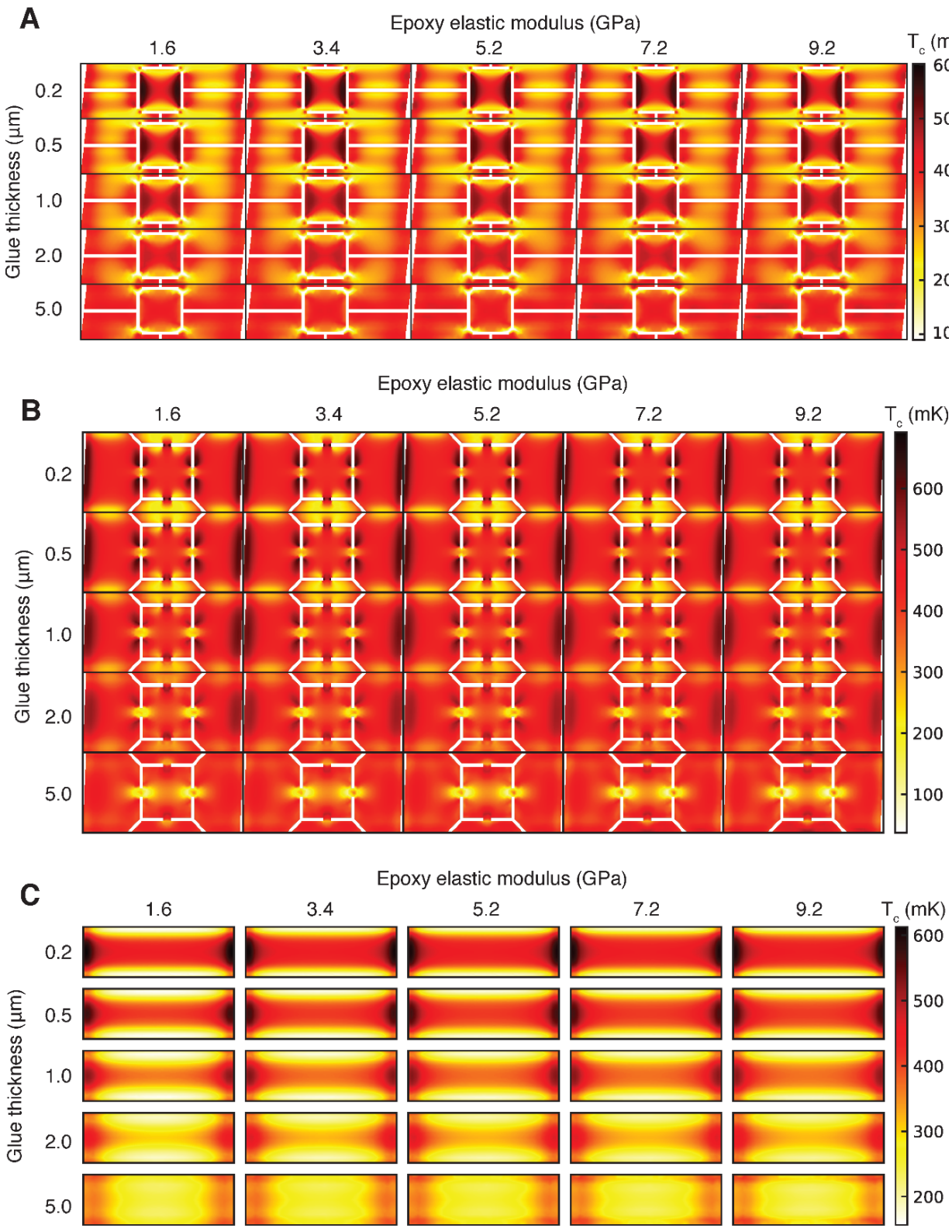
A
Epoxy elastic modulus (GPa)
1.6
3.4
5.2
7.2
9.2
Glue thickness (µm)
0.2
0.5
1.0
2.0
5.0
B
Epoxy elastic modulus (GPa)
1.6
3.4
5.2
7.2
9.2
T_c (mK)
600
500
400
300
200
100
Glue thickness (µm)
0.2
0.5
1.0
2.0
5.0
C
Epoxy elastic modulus (GPa)
1.6
3.4
5.2
7.2
9.2
T_c (mK)
600
500
400
300
200
Glue thickness (µm)
0.2
0.5
1.0
2.0
5.0

Fig. S9

Dependence of T_c maps on epoxy parameters for (A) device 1, (B) device 2 and (C) the unprocessed lamella. The strain field is calculated for different combinations of the epoxy thickness and elastic modulus. For each combination of epoxy parameters, a T_c map is generated using the procedure described above. The room temperature modulus of the epoxy is ≈ 3.4 GPa and the cryogenic modulus of the epoxy is ≈ 7.2 GPa (30). We test values for the epoxy modulus that exceed these limits, showing that for physically reasonable values, the structure of the superconducting transition is preserved. The thickness of the glue is increased from 0.2 μm up to 5 μm, demonstrating the relaxation of the strain field as the epoxy layer increases.

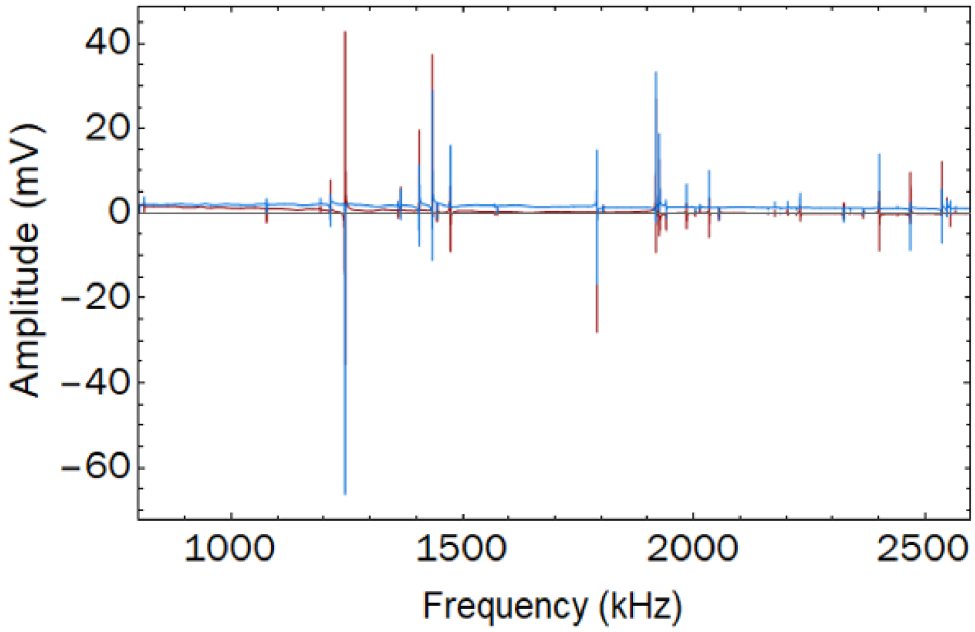

Fig. S10

Resonant ultrasound spectrum of $CeIrIn_5$. In-phase (red) and out-of-phase (blue) ultrasonic response of a single crystal of $CeIrIn_5$ showing the first 40 mechanical resonances. The resonant frequencies are used to compute the elastic moduli of $CeIrIn_5$.

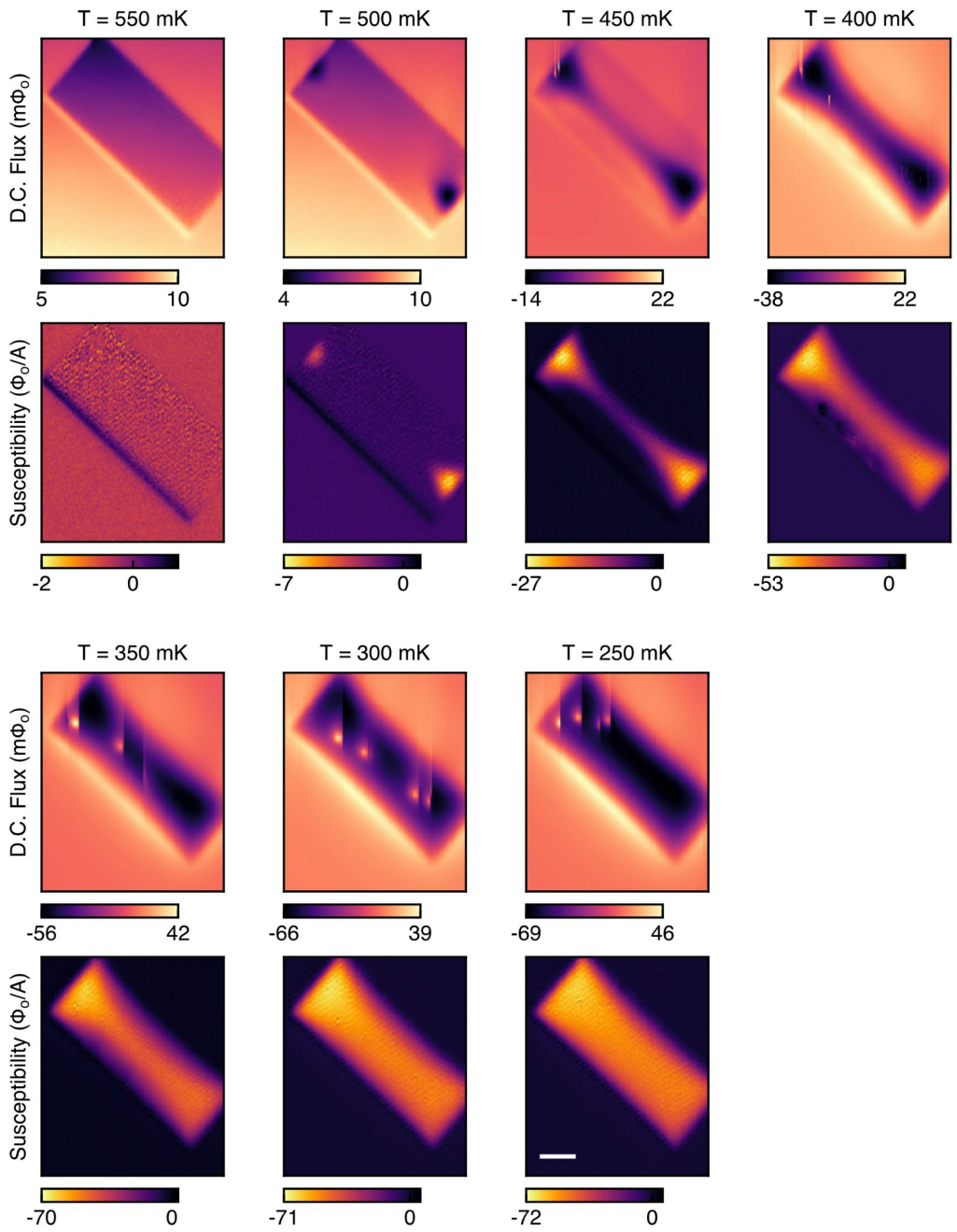

Fig. S11

Series of scanning SQUID images taken while cooling through the superconducting transition. Scale bar 25 μm. DC Magnetometry (top) records the flux threading the SQUID loop as it scans over the sample surface. Meissner screening of the ambient magnetic field in the cryostat above the superconducting regions of the sample are shown as dark shadows in the DC images. Stationary superconducting vortices appear as bright spots embedded in the superconducting regions of the sample. Vortex motion during the scan causes bright vertical streaking in the image. Magnetic susceptibility (bottom) shows development of superconductivity in the sample in greater detail than in the main text.

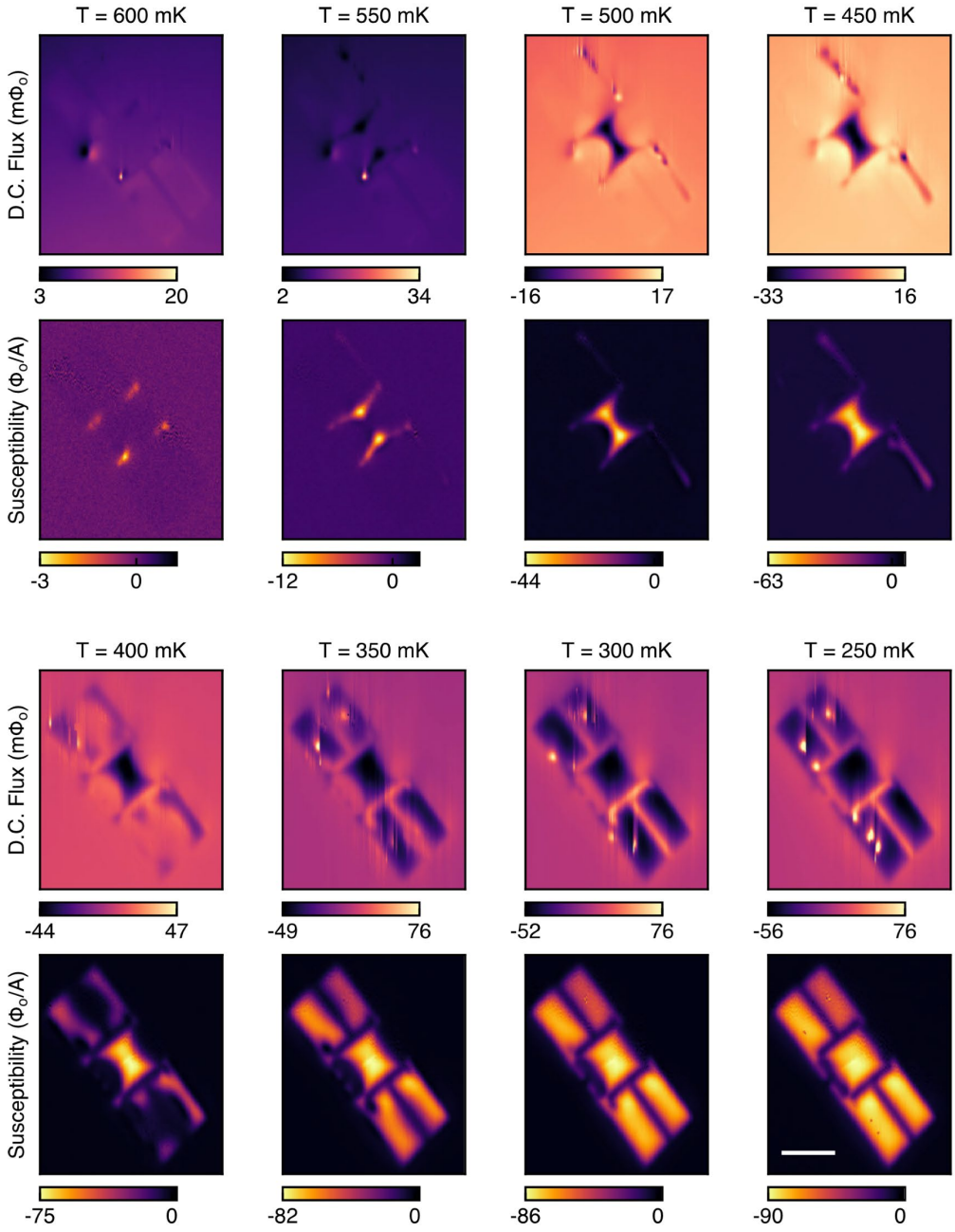

Fig. S12

Series of scanning SQUID images taken while cooling through the superconducting transition in device 1. Scale bar 25 μm. DC Magnetometry (top) records the flux threading the SQUID loop as it scans over the sample surface. Meissner screening of the ambient magnetic field in the cryostat above the superconducting regions of the sample are shown as dark shadows in the DC images. Stationary superconducting vortices appear as bright spots embedded in the superconducting regions of the sample. Vortex motion during the scan causes bright vertical streaking in the image. Magnetic susceptibility (bottom) shows development of superconductivity in the sample in greater detail than in the main text.

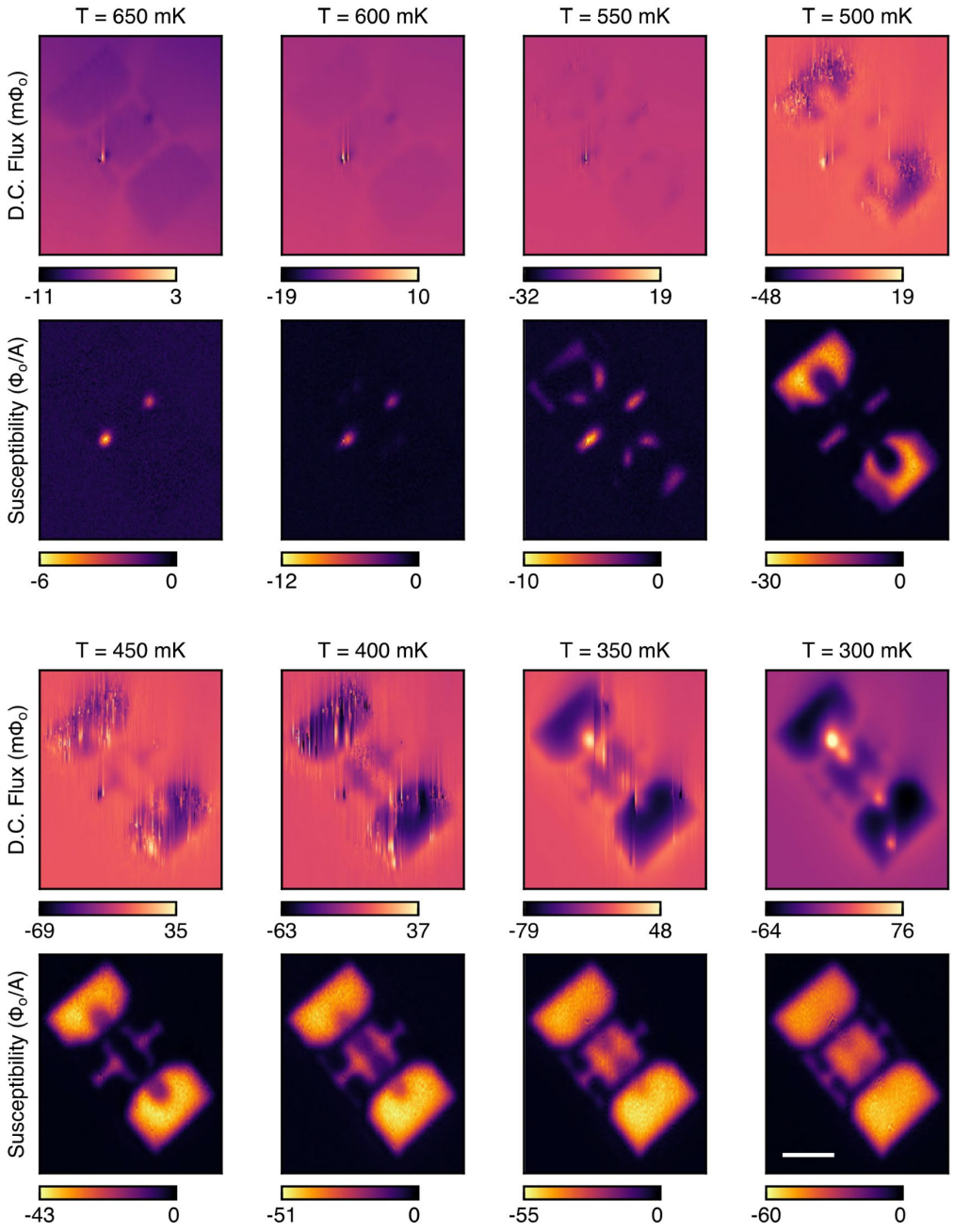

Fig. S13

Series of scanning SQUID images taken while cooling through the superconducting transition in device 2. Scale bar 30 μm. DC Magnetometry (top) records the flux threading the SQUID loop as it scans over the sample surface. Meissner screening of the ambient magnetic field in the cryostat above the superconducting regions of the sample are shown as dark shadows in the DC images. Stationary superconducting vortices appear as bright spots embedded in the superconducting regions of the sample. Vortex motion during the scan causes bright vertical streaking in the image. Magnetic susceptibility (bottom) shows the development of superconductivity in the sample in greater detail than in the main text.

Table S1.

Material properties used in the finite element method simulations of the strain field.

Property	Value
Total thermal contraction of $CeIrIn_5$	$\varepsilon_{ao} = -3.2 \times 10^{-3}$, $\varepsilon_{co} = -3.5 \times 10^{-3}$
Total thermal contraction of sapphire	$\varepsilon_o = -8 \times 10^{-4}$ (37)
Young's moduli $CeIrIn_5$	$E_a = 129\ GPa\ E_c = 109\ GPa$
Young's modulus epoxy	7.2 GPa (30)
Young's modulus sapphire	470 GPa (37)

Table S2.

Room temperature elastic moduli of $CeIrIn_5$ measured by resonant ultrasound.

Elastic Modulus	C_{11}	C_{33}	C_{13}	C_{12}	C_{44}	C_{66}
Value (GPa)	153.1	138.8	53.1	41.3	46.3	42.0

References and Notes

1. C. W. Hicks, D. O. Brodsky, E. A. Yelland, A. S. Gibbs, J. A. N. Bruin, M. E. Barber, S. D. Edkins, K. Nishimura, S. Yonezawa, Y. Maeno, A. P. Mackenzie, Strong increase of T_c of Sr_2RuO_4 under both tensile and compressive strain. *Science* **344**, 283–285 (2014). doi:10.1126/science.1248292 Medline

2. A. E. Böhmer, A. Sapkota, A. Kreyssig, S. L. Bud'ko, G. Drachuck, S. M. Saunders, A. I. Goldman, P. C. Canfield, Effect of Biaxial Strain on the Phase Transitions of $Ca(Fe_{1-x}Co_x)_2As_2$. *Phys. Rev. Lett.* **118**, 107002 (2017). doi:10.1103/PhysRevLett.118.107002 Medline

3. C. Petrovic, R. Movshovich, M. Jaime, P. G. Pagliuso, M. F. Hundley, J. L. Sarrao, Z. Fisk, J. D. Thompson, A new heavy-fermion superconductor $CeIrIn_5$: A relative of the cuprates? *Europhys. Lett.* **53**, 354–359 (2001). doi:10.1209/epl/i2001-00161-8

4. Y. Haga, Y. Inada, H. Harima, K. Oikawa, M. Murakawa, H. Nakawaki, Y. Tokiwa, D. Aoki, H. Shishido, S. Ikeda, N. Watanabe, Y. Ōnuki, Quasi-two-dimensional Fermi surfaces of the heavy fermion superconductor $CeIrIn_5$. *Phys. Rev. B* **63**, 060503(R) (2001). doi:10.1103/PhysRevB.63.060503

5. O. M. Dix, A. G. Swartz, R. J. Zieve, J. Cooley, T. R. Sayles, M. B. Maple, Anisotropic dependence of superconductivity on uniaxial pressure in $CeIrIn_5$. *Phys. Rev. Lett.* **102**, 197001 (2009). doi:10.1103/PhysRevLett.102.197001 Medline

6. N. Oeschler, P. Gegenwart, M. Lang, R. Movshovich, J. L. Sarrao, J. D. Thompson, F. Steglich, Uniaxial pressure effects on $CeIrIn_5$ and $CeCoIn_5$ studied by low-temperature thermal expansion. *Phys. Rev. Lett.* **91**, 076402 (2003). doi:10.1103/PhysRevLett.91.076402 Medline

7. R. Borth, E. Lengyel, P. G. Pagliuso, J. L. Sarrao, G. Sparn, F. Steglich, J. D. Thompson, Heat capacity of the heavy fermion superconductor $CeIrIn_5$ under hydrostatic pressure. *Physica B* **312–313**, 136–137 (2002). doi:10.1016/S0921-4526(01)01085-7

8. P. J. W. Moll, B. Zeng, L. Balicas, S. Galeski, F. F. Balakirev, E. D. Bauer, F. Ronning, Field-induced density wave in the heavy-fermion compound $CeRhIn_5$. *Nat. Commun.* **6**, 6663 (2015). doi:10.1038/ncomms7663 Medline

9. F. Ronning, T. Helm, K. R. Shirer, M. D. Bachmann, L. Balicas, M. K. Chan, B. J. Ramshaw, R. D. McDonald, F. F. Balakirev, M. Jaime, E. D. Bauer, P. J. W. Moll, Electronic in-plane symmetry breaking at field-tuned quantum criticality in $CeRhIn_5$. *Nature* **548**, 313–317 (2017). doi:10.1038/nature23315 Medline

10. See supplementary materials.

11. R. S. Kumar, H. Kohlmann, B. E. Light, A. L. Cornelius, V. Raghavan, T. W. Darling, J. L. Sarrao, Anisotropic elastic properties of $CeRhIn_5$. *Phys. Rev. B* **69**, 014515 (2004). doi:10.1103/PhysRevB.69.014515

12. M. Tinkham, *Introduction to Superconductivity* (Dover, 2004).

13. H. C. Montgomery, Method for measuring electrical resistivity of anisotropic materials. *J. Appl. Phys.* **42**, 2971–2975 (1971). doi:10.1063/1.1660656

14. L. J. van der Pauw, A method of measuring the resistivity and Hall coefficient on lamellae of arbitrary shape. *Philips Tech. Rev.* **20**, 220–224 (1958).

15. S. Wüchner, N. Keller, J. L. Tholence, J. Flouquet, Magnetic properties of the heavy-fermion superconductors UPt_3 and URu_2Si_2. *Solid State Commun.* **85**, 355–360 (1993). doi:10.1016/0038-1098(93)90032-I

16. A. Pollini, A. C. Mota, P. Visani, R. Pittini, G. Juri, T. Teruzzi, Flux dynamics and low-field magnetic properties of the heavy-fermion superconductor $CeCu_2Si_2$. *J. Low Temp. Phys.* **90**, 15–53 (1993). doi:10.1007/BF00682009

17. H. Shishido, R. Settai, D. Aoki, S. Ikeda, H. Nakawaki, N. Nakamura, T. Iizuka, Y. Inada, K. Sugiyama, T. Takeuchi, K. Kindo, T. C. Kobayashi, Y. Haga, H. Harima, Y. Aoki, T. Namiki, H. Sato, Y. Ōnuki, Fermi surface, magnetic and superconducting properties of $LaRhIn_5$ and $CeTIn_5$ (T: Co, Rh and Ir). *J. Phys. Soc. Jpn.* **71**, 162–173 (2002). doi:10.1143/JPSJ.71.162

18. T. Shang, R. E. Baumbach, K. Gofryk, F. Ronning, Z. F. Weng, J. L. Zhang, X. Lu, E. D. Bauer, J. D. Thompson, H. Q. Yuan, $CeIrIn_5$: Superconductivity on a magnetic instability. *Phys. Rev. B* **89**, 041101(R) (2014). doi:10.1103/PhysRevB.89.041101

19. S. Nair, M. Nicklas, J. L. Sarrao, J. D. Thompson, F. Steglich, S. Wirth, Analysis of the normal-state magnetotransport in $CeIrIn_5$. *J. Supercond. Nov. Magn.* **22**, 195–199 (2009). doi:10.1007/s10948-008-0379-z

20. S. Wirth, Y. Prots, M. Wedel, S. Ernst, S. Kirchner, Z. Fisk, J. D. Thompson, F. Steglich, Y. Grin, Structural investigations of $CeIrIn_5$ and $CeCoIn_5$ on macroscopic and atomic length scales. *J. Phys. Soc. Jpn.* **83**, 061009 (2014). doi:10.7566/JPSJ.83.061009

21. S. Nair, M. Nicklas, F. Steglich, J. L. Sarrao, J. D. Thompson, A. J. Schofield, S. Wirth, Precursor state to superconductivity in $CeIrIn_5$: Unusual scaling of magnetotransport. *Phys. Rev. B* **79**, 094501 (2009). doi:10.1103/PhysRevB.79.094501

22. A. Bianchi, R. Movshovich, M. Jaime, J. D. Thompson, P. G. Pagliuso, J. L. Sarrao, Origin of the zero-resistance anomaly in heavy fermion superconducting $CeIrIn_5$: A clue from magnetic-field and Rh-doping studies. *Phys. Rev. B* **64**, 220504(R) (2001). doi:10.1103/PhysRevB.64.220504

23. J. Wu, I. Božović, Perspective: Extremely fine tuning of doping enabled by combinatorial molecular-beam epitaxy. *APL Mater.* **3**, 062401 (2015). doi:10.1063/1.4917283

24. H. Shishido, R. Settai, H. Harima, Y. Onuki, A Drastic Change of the Fermi Surface at a Critical Pressure in $CeRhIn_5$: dHvA Study under Pressure. *J. Phys. Soc. Jpn.* **74**, 1103–1106 (2005). doi:10.1143/JPSJ.74.1103

25. M. D. Bachmann *et al*., Data for "Spatial control of heavy-fermion superconductivity in $CeIrIn_5$." Zenodo (2019); doi: 10.5281/zenodo.3462534.

26. M. E. Huber, N. C. Koshnick, H. Bluhm, L. J. Archuleta, T. Azua, P. G. Björnsson, B. W. Gardner, S. T. Halloran, E. A. Lucero, K. A. Moler, Gradiometric micro-SQUID susceptometer for scanning measurements of mesoscopic samples. *Rev. Sci. Instrum.* **79**, 053704 (2008). doi:10.1063/1.2932341 Medline

27. B. J. Ramshaw, A. Shekhter, R. D. McDonald, J. B. Betts, J. N. Mitchell, P. H. Tobash, C. H. Mielke, E. D. Bauer, A. Migliori, Avoided valence transition in a plutonium superconductor. *Proc. Natl. Acad. Sci. U.S.A.* **112**, 3285–3289 (2015). doi:10.1073/pnas.1421174112 Medline

28. W. M. Visscher, A. Migliori, T. M. Bell, R. A. Reinert, On the normal modes of free vibration of inhomogeneous and anisotropic elastic objects. *J. Acoust. Soc. Am.* **90**, 2154–2162 (1991). doi:10.1121/1.401643

29. COMSOL Mutiphysics, v. 5.3a, COMSOL AB; www.comsol.com.

30. K. Dahlerup-Petersen, A. Perrot, "Properties of organic composite materials at cryogenic temperatures" (Report ISR-BOM-79-39, CERN, 1979); https://cds.cern.ch/record/312298.

31. M. Nicklas, V. A. Sidorov, H. A. Borges, P. G. Pagliuso, J. L. Sarrao, J. D. Thompson, Two superconducting phases in $CeRh_{1-x}Ir_xIn_5$. *Phys. Rev. B* **70**, 020505 (2004). doi:10.1103/PhysRevB.70.020505

32. H. Yaguchi, M. Wada, T. Akima, Y. Maeno, T. Ishiguro, Interface superconductivity in the eutectic Sr_2RuO_4 - Ru: 3-K phase of Sr_2RuO_4. *Phys. Rev. B* **67**, 214519 (2003). doi:10.1103/PhysRevB.67.214519

33. M. Sigrist, K. Ueda, Phenomenological theory of unconventional superconductivity. *Rev. Mod. Phys.* **63**, 239–311 (1991). doi:10.1103/RevModPhys.63.239

34. K. An, T. Sakakibara, R. Settai, Y. Onuki, M. Hiragi, M. Ichioka, K. Machida, Sign reversal of field-angle resolved heat capacity oscillations in a heavy Fermion superconductor $CeCoIn_5$ and d_{x2-y2} pairing symmetry. *Phys. Rev. Lett.* **104**, 037002 (2010). doi:10.1103/PhysRevLett.104.037002 Medline

35. Y. Kasahara, T. Iwasawa, Y. Shimizu, H. Shishido, T. Shibauchi, I. Vekhter, Y. Matsuda, Thermal conductivity evidence for a $d_{x^2-y^2}$ pairing symmetry in the heavy-fermion $CeIrIn_5$ superconductor. *Phys. Rev. Lett.* **100**, 207003 (2008). doi:10.1103/PhysRevLett.100.207003 Medline

36. D. Vandervelde, H. Q. Yuan, Y. Onuki, M. B. Salamon, Evidence of d-wave pairing symmetry of the gap of the heavy-fermion superconductor $CeIrIn_5$ from magnetic-penetration-depth measurements. *Phys. Rev. B* **79**, 212505 (2009). doi:10.1103/PhysRevB.79.212505

37. J. Ekin, *Experimental Techniques for Low-Temperature Measurements: Cryostat Design, Material Properties and Superconductor Critical-Current Testing* (Oxford Univ. Press, 2006).